



# The combination of electrospinning and forcespinning: Effects on a viscoelastic jet and a single nanofiber

Wei-Min Chang<sup>a</sup>, Cheng-Chien Wang<sup>b</sup>, Chuh-Yung Chen<sup>a,c,\*</sup>

<sup>a</sup> Department of Chemical Engineering, National Cheng Kung University, No. 1, Daxue Rd., East Dist., Tainan City 70101, Taiwan, ROC

<sup>b</sup> Department of Chemical and Materials Engineering, Southern Taiwan University, No. 1, Nantai St., Yongkang Dist., Tainan City 71005, Taiwan, ROC

<sup>c</sup> Research Center for Energy Technology and Strategy, National Cheng Kung University, No. 1, Daxue Rd., East Dist., Tainan City 70101, Taiwan, ROC

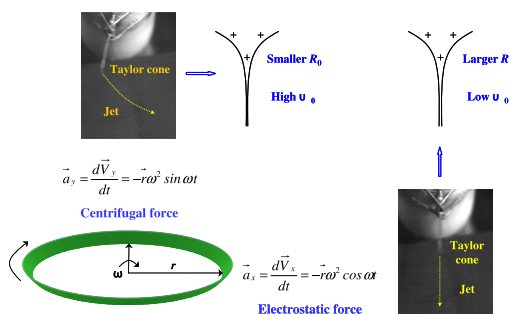


## HIGHLIGHTS

- Novel electrospinning technique which combines electrospinning and forcespinning was proposed.
- A viscoelastic jet has a strong stretching and a fast extension speed force under electrostatic and centrifugal forces.
- This technique can remove “whipping instability” and fabricate a series of uniaxially aligned polymeric nanofibers.
- Dimensionless groups determine the jet behavior and physical properties of polymeric nanofibers.

## GRAPHICAL ABSTRACT

The combination of electrospinning and forcespinning (or called electrostatic-centrifugal spinning) was first proposed in our laboratory. A strong stretching force and a fast extension speed will form after optimizing the curvature radius (by  $Re$  and  $We$  numbers), jet length (by  $Pe$  and  $\varepsilon$  numbers), and Taylor cone (by  $\Pi_1$  and  $Oh$  numbers). Furthermore, the  $Re$ ,  $\Pi_1$  and  $Oh$  numbers was used to explore the relationship of jet behavior, product morphology (e.g., beads, beaded fibers, and nanofibers), and physical property (e.g., conformation, molecular orientation, crystallinity, hardness, and elastic modulus), and further fabricate a series of functional polymeric nanofibers. These innovative model, novel technique, and functional material will be able to open a major milestone in nanoscience and nanotechnology.



## ARTICLE INFO

### Article history:

Received 6 November 2013

Received in revised form 28 January 2014

Accepted 1 February 2014

Available online 7 February 2014

### Keywords:

Electrospinning

Forcespinning

Nanofibers

Dimensionless

## ABSTRACT

The combination of electrospinning and forcespinning (otherwise called electrostatic-centrifugal spinning) was first proposed in our laboratory. A viscoelastic jet has a stretching force in the axial ( $\vec{a}_x$ ) and tangential ( $\vec{a}_y$ ) directions under electrostatic and centrifugal forces. The jet radius ( $R_0$ ) will be dramatically decreased, and the jet velocity ( $v_0$ ) will be substantially increased due to a particular stretching force. The radius of curvature, the jet length, and the Taylor cone of a viscoelastic jet will be completely different when the jet velocity ( $v_0$ ) increases. A strong stretching force and a fast extension speed will form after optimizing the radius of curvature (by Reynolds ( $Re$ ) and Weber ( $We$ ) numbers), jet length (by Peclet ( $Pe$ ) and Epsilon ( $\varepsilon$ ) numbers), and Taylor cone (by dimensionless stress ( $\Pi_1$ ) and Ohnesorge ( $Oh$ ) numbers). Through dimensionless number and group analysis, higher  $Re$  ( $PC = 9.38 \times 10^{-2}$ ,  $PLA = 1.52 \times 10^{-1}$  and  $PAN = 1.53 \times 10^{-2}$ ) and  $We$  ( $PC = 13.8$ ,  $PLA = 15$  and  $PAN = 13.3$ ) number of all three systems can collect the bead-free and uniform nanofibers. Similarly, higher  $\Pi_1$  ( $PC = 1.83 \times 10^{-5}$ ,  $PLA = 2.86 \times 10^{-5}$  and  $PAN = 5.13 \times 10^{-9}$ ) and  $Oh$  ( $PC = 39.60$ ,  $PLA = 29.22$  and  $PAN = 238.94$ ) numbers

\* Corresponding author at: Department of Chemical Engineering, National Cheng Kung University, No. 1, Daxue Rd., East Dist., Tainan City 70101, Taiwan, ROC. Tel.: +886 6 2360468; fax: +886 6 2344496.

E-mail address: [ccy7@ccmail.ncku.edu.tw](mailto:ccy7@ccmail.ncku.edu.tw) (C.-Y. Chen).

refer to viscosity and electrostatic force dominate the jet behavior and obtained the nanofiber with high modulus, hardness, crystallinity and good molecular orientation. Hence, the uniaxially aligned polycarbonate, polylactic acid and polyacrylonitrile nanofibers with superior physical properties (modulus  $\geq 2.77$  GPa, 3.3 GPa and 1.46 GPa, hardness  $\geq 0.32$ , 0.26 and 0.22 and crystallinity  $\geq 3\%$ , 37% and 21%) can be successfully manufactured in this process.

© 2014 Elsevier B.V. All rights reserved.

## Nomenclature

$\eta_0$	viscosity of solution
$R_0$	jet radius
$\gamma$	surface tension of solution
$v_0$	velocity of jet
$K$	conductivity
$E_0$	electric field
$\rho$	density
$\bar{\epsilon}$	air dielectric ( $8.854 \times 10^{-12}$ )
$Re$	$\frac{\rho \cdot v_0 \cdot R_0}{\eta_0}$ (Reynolds number)

$We$	$\frac{\rho \cdot v_0^2 \cdot R_0}{\gamma}$ (Weber number)
$Pe$	$\frac{2 \cdot \bar{\epsilon} \cdot v_0}{K \cdot R_0}$ (Peclet number)
$\epsilon$	$\frac{\bar{\epsilon} \cdot E_0^2}{\rho \cdot v_0}$ (Epsilon number)
$\Pi_1$	$Re \cdot Pe \cdot \epsilon = \frac{2 \cdot \bar{\epsilon} \cdot E_0^2}{K \cdot \eta_0}$ (Dimensionless group)
$Oh$	$Re^{-1} \cdot We^{\frac{1}{2}} = \frac{\eta_0}{\sqrt{\rho \cdot \gamma \cdot R_0}}$ (Dimensionless group)

## 1. Introduction

Electrospinning [1], or Forcespinning™ [2,3], is a technique whereby a strong electrostatic field or centrifugal field is used to accelerate and elongate a viscoelastic jet, allowing the production of polymeric nanofibers. These thin fibers have a variety of current and potential applications in energy and electronics [4], environmental engineering and biotechnology [5], bioengineering [6–9], defense and security [10,11], processing [1], and characterization [12], among other fields. Therefore, many scholars [2,3,13–21] are continuously developing or designing novel electrospinning techniques to manufacture or fabricate functional polymeric nanofibers. However, these techniques (e.g., specific collector [13–18], multiple spinneret [19,20], and Forcespinning™ [2,3]) still can neither improve the motor behavior of a viscoelastic jet nor enhance the physical properties of a single nanofiber. Therefore, optimizing the motor behavior of a viscoelastic jet and inducing the anisotropic structural properties of a single nanofiber will have unlimited potential in the future.

Since 1969, Taylor [22] has found that two distinct stages, a “stable jet” phase and a “whipping instability” phase, exist in the electrospinning process. Between 1997 and 2001, several analytical models for electrospinning based on slender body electrodynamic theory [23], a power-law viscosity [24], Newtonian viscosity [25,26], and the linear Maxwell equation [27,28] were proposed to predict jet behavior [29–31]. In 1998, Spivak et al. [24] proposed the first model for the “stable jet” profile. In their model, the jet momentum equation (including a term for the electrical force on the jet), jet continuity equation, and electric field equation are coupled together, and the resultant model can be solved for the expected jet radius profile as the jet moves away from the spinneret. In 2001, Hohman et al. [25,26] used a similar approach to model the stable jet region, and furthermore conducted a linear stability analysis that considered jet motion away from the axisymmetric centerline of the jet. This analysis allowed the onset of whipping instability to be examined under the assumption that the fluids are Newtonian. The viscoelasticity of the fluids was not considered in the analysis. In 2000 and 2001, Reneker et al. [27] and Yarin et al. [28] proposed the second model for the “whipping instability” profile. In this approach, the electrospun jet is considered to be a series of discrete charged beads connected by viscoelastic springs. A major advantage of this type of

approach is that the discretization of the jet allows the trajectory of the bending instability to be followed as it develops. The instability trajectories obtained from this analysis are similar in character to those observed experimentally. However, these models all involve internal parameters whose values are impossible to know a priori and are very difficult to measure in practice.

On the other hand, since 2002, Matthews et al. [32] has found that the degree of collagen fiber uniaxial alignment will be enhanced when the rotating speed of the mandrel increases to 4500 rpm. In addition, the peak stress ( $1.5 \pm 0.2$  MPa) and average modulus ( $52.3 \pm 5.2$  MPa) for the axial direction of collagen fibers are higher than those values for the horizontal direction (peak stress =  $0.7 \pm 0.1$  MPa and average modulus =  $26.1 \pm 4.0$  MPa). In 2007, Kakade et al. [33] used a parallel aluminum flat plate to enhance the degree of uniaxial alignment and molecular orientation in polyethylene oxide (PEO) nanofibers under an electrostatic field. Similarly, in 2008, Kongkhleng et al. [34] used a rotating disk to control the crystal morphology and molecular orientation of polyoxymethylene (POM) nanofibers under an electrostatic field. It is clear that these techniques are all used with a negative electrode possessing a strong external force [32,34] or with a directional arrangement [33] to drive the arrangement of the thinning jet on the collector. When a “stable jet” is initiated from a Taylor cone under an electrostatic field, “whipping instability” will appear, and the severe spiral swing will cause the jet to be continuously thinned; finally, the thin fibers with a positive charge will be formed with a uniaxial alignment closer to the negatively charged collector. However, these techniques (e.g., specific collector [13–18], multiple spinneret [19,20], and Forcespinning™ [2,3]) still cannot successfully induce anisotropic structural properties (mechanical, electrical, etc.) in a polymeric nanofiber with low crystallinity (e.g., PC and PAN) or a slow crystallization rate (e.g., PLA). The reason is that the “whipping instability” caused by the degree of the polymer chains parallel to the fiber axis substantially drops during the electrospinning process [1,33,34]. Thus, the “whipping instability” is still a problem for the current electrospinning technique [2,3,13–21,32–34]. In addition, the relationships between the jet behavior, product morphology, and physical properties has not yet been clarified. Therefore, optimizing the motor behavior of a viscoelastic jet and inducing the conformation of a single nanofiber at each stage of electrospinning becomes a very interesting topic.

Hence, this study attempted to develop a novel technique to solve the problems described above. In 2002, Feng [35] studied the electrostatics, fluid mechanics, rheology, and role of viscoelasticity and proposed a slender-body theory for the stretching of a straight charged jet of a Giesekus fluid. Moreover, Feng [35] identified several dimensionless numbers (Peclet ( $Pe$ ), Reynolds ( $Re$ ), Weber ( $We$ ), and Epsilon ( $\epsilon$ ) numbers) as governing parameters for electrospinning in a model developed from the conservation equations for mass, momentum, and electrical charge applied to an electrospinning jet of a Newtonian fluid. To eliminate the internal variables in a dimensional analysis of the electrospinning of a Newtonian fluid, Helgeson and Wagner [36] provided a robust correlation between the dimensionless fiber radius, as characterized by the Ohnesorge ( $Oh$ ) number, and a new dimensionless group,  $\Pi_1$ , which relates controllable operating parameters and measurable solution spinning properties. From the above findings, the dimensionless numbers ( $Pe$ ,  $Re$ ,  $We$ , and  $\epsilon$  numbers) and dimensionless groups ( $\Pi_1$  and  $Oh$  numbers) were used to clearly observe the behavior of a viscoelastic jet (e.g., radius of curvature, jet length, and Taylor cone). It is noteworthy that the combination of electrospinning and forcespinning (otherwise called electrostatic-centrifugal spinning) was first proposed in our laboratory [37–40]. The combination of electrospinning and forcespinning can substantially enhance the inertial stress (by  $Re$  and  $We$  numbers), electrical convection (by  $Pe$  and  $\epsilon$  numbers), and viscous stress (by  $\Pi_1$  and  $Oh$  numbers) of a viscoelastic jet, further creating a strong stretching force and a fast extension speed. The combination of electrospinning and forcespinning can produce unique jet behavior that further removes “whipping instability”. Furthermore, a viscoelastic jet with electrostatic and centrifugal forces can also determine the product morphology of and further induce anisotropic structural properties (e.g., conformation, molecular orientation, crystallinity, hardness, and modulus) in polymeric nanofibers. This novel technique, and these functional materials will constitute a major milestone in the areas of nanoscience and nanotechnology.

## 2. Experimental

### 2.1. Materials

Acetone ( $(\text{CH}_3)_2\text{CO}$ , Aldrich Co. Ltd.), chloroform ( $\text{CHCl}_3$ , Aldrich Co. Ltd.), dichloromethane ( $\text{CH}_2\text{Cl}_2$ , Aldrich Co. Ltd.), tetrahydrofuran (THF, Aldrich Co. Ltd.), and  $N,N$ -dimethylformamide (DMF, Aldrich Co. Ltd.) were used as received.

Polycarbonate (PC) resin pellets with an average molecular weight ( $M_w$ ) of 168,000 g/mol (Chi-Lin Technology Co., Ltd), polylactic acid (PLA) resin pellets with  $M_w$  of 100,000 g/mol (Chi-Mei Corporation Co., Ltd.), and polyacrylonitrile (PAN) with  $M_w$  of 150,000 g/mol [41] were dissolved in single- or co-solvent, as listed in Tables 1–3.

### 2.2. Equipment

A polymer solution was placed into a 50-mL syringe attached to a horizontally mounted syringe pump (kdScientific KDS-100). The potential was applied to the upper surface of a PTFE tube (outer diameter = 6 cm) using a high-voltage power supply (Pebio CE-LIF). Voltage was conducted via an interior copper pipe and then run through the upper surface of a PTFE tube to the end of the needle. A grounded copper ring (inner diameter = 50 cm) was used as the target. The detail schematic diagram was shown in our previous study [39]. The spinning conditions for each polymer solution are shown in Tables 1–3.

### 2.3. Analysis

A zero-shear viscosity meter (Brookfield LVDV-I+), a conductivity meter (Trans Instruments WalkLAB A Microcontroller with LSI Technology Automatic Temperature Compensation, range: 0.1  $\mu\text{S}$  to 100.0 mS), and a surface-tension meter (FACE surface tensiometer CBVP-A3) were used to measure the solution properties at 25 °C and 68% relative humidity. A high-speed charge-coupled device (CCD; IDT XS-4) camera was used to observe the viscoelastic jet emitted from the bottom of Taylor cone. Images were captured at a rate of the 10,000 frames/s.

The elastic properties of submicro- and nanofibers were measured with a three-point bend test [42–46]. In this test, a single nanofiber was suspended over an empty space, and a small deflection was applied to the middle of the nanofiber along its length with an atomic-force microscopy cantilever (Agilent Technologies P\* PicoPlus) in contact mode. A schematic diagram of the three-point bend test and AFM-scanned cross-sectional profiles were provided in our previous study [38]. To confirm the accuracy of the three-point bend test, the elastic-plastic nanoindentation test [47–51] was used to determine the hardness ( $H$ ) and reduced elastic (Young's) modulus ( $E_r$ ) of the near-surface region of the material. The MTS-Nanoindenter-XP (MTS-XP) apparatus uses a compliance indentation system capable of operating at loads in the microgram range. The theoretical resolution of the instrument

**Table 1**  
Dimensionless (groups) and mechanical properties of PC nanofibers fabricated under the different operational conditions.

Operational variables	Peclet number ( $Pe$ )	Reynolds number ( $Re$ )	Weber number ( $We$ )	Epsilon number ( $\epsilon$ )	Dimensionless stress ( $\Pi_1$ )	Ohnesorge number ( $Oh$ )	Modulus (GPa) <sup>c</sup>	Modulus (GPa) <sup>d</sup>
25 °C <sup>a</sup>	5 kV	$5.64 \times 10^{-3}$	$4.17 \times 10^{-2}$	$1.21 \times 10^{+0}$	$3.03 \times 10^{-3}$	$7.13 \times 10^{-7}$	26.40	0.01
	10 kV	$7.22 \times 10^{-3}$	$4.53 \times 10^{-2}$	$1.55 \times 10^{+0}$	$3.03 \times 10^{-3}$	$9.92 \times 10^{-7}$	27.52	0.04
	15 kV	$1.06 \times 10^{-2}$	$5.15 \times 10^{-2}$	$2.29 \times 10^{+0}$	$3.03 \times 10^{-3}$	$1.66 \times 10^{-6}$	29.35	0.52
	20 kV	$1.65 \times 10^{-2}$	$5.97 \times 10^{-2}$	$3.56 \times 10^{+0}$	$3.03 \times 10^{-3}$	$3.00 \times 10^{-6}$	31.59	2.86
	25 kV	$6.42 \times 10^{-2}$	$9.38 \times 10^{-2}$	$1.38 \times 10^{+1}$	$3.03 \times 10^{-3}$	$1.83 \times 10^{-5}$	39.60	7.11
	30 kV	$2.20 \times 10^{-2}$	$6.57 \times 10^{-2}$	$4.74 \times 10^{+0}$	$3.03 \times 10^{-3}$	$4.39 \times 10^{-6}$	33.14	2.11
25 kV <sup>b</sup>	25 °C	$6.42 \times 10^{-2}$	$9.38 \times 10^{-2}$	$1.38 \times 10^{+1}$	$3.03 \times 10^{-3}$	$1.83 \times 10^{-5}$	39.60	7.11
	30 °C	$5.13 \times 10^{-3}$	$4.04 \times 10^{-2}$	$1.10 \times 10^{+0}$	$3.03 \times 10^{-3}$	$6.29 \times 10^{-7}$	25.99	$1.11 \times 10^{-3}$
	35 °C	$2.75 \times 10^{-3}$	$3.28 \times 10^{-2}$	$5.92 \times 10^{-1}$	$3.03 \times 10^{-3}$	$2.74 \times 10^{-7}$	23.43	$1.58 \times 10^{-4}$
	40 °C	$1.64 \times 10^{-3}$	$2.77 \times 10^{-2}$	$3.54 \times 10^{-1}$	$3.03 \times 10^{-3}$	$1.38 \times 10^{-7}$	21.50	$9.89 \times 10^{-5}$
	45 °C	$7.21 \times 10^{-4}$	$2.10 \times 10^{-2}$	$1.55 \times 10^{-1}$	$3.03 \times 10^{-3}$	$4.60 \times 10^{-8}$	18.74	$1.70 \times 10^{-6}$
								–

<sup>a</sup> The PC products were fabricated at a concentration (Conc.) of 14 wt%, a flow rate (FR) of 0.25 mL/h, a spinneret tip-to-collector distance (TCD) of 20 cm, a temperature ( $T$ ) of 25 °C, and an additional centrifugal field (CF) of 1800 rpm.

<sup>b</sup> The PC products were fabricated at Conc. = 14 wt%, FR = 0.25 mL/h, TCD = 20 cm, and EF = 25 kV, with CF = 1800 rpm.

<sup>c</sup> Nanoscale three-point bend test measured by AFM.

<sup>d</sup> Elastic-plastic nanoindentation test measured by nanoindenter.

**Table 2**

Dimensionless (groups) and mechanical properties of PLA nanofibers fabricated under the different operational conditions.

Operational variables		Peclet number ( $Pe$ )	Reynolds number ( $Re$ )	Weber number ( $We$ )	Epsilon number ( $\varepsilon$ )	Dimensionless stress ( $\Pi_1$ )	Ohnesorge number ( $Oh$ )	Modulus (GPa) <sup>c</sup>	Modulus (GPa) <sup>d</sup>
PLA in CH <sub>2</sub> Cl <sub>2</sub> /THF (1/1) <sup>a</sup>	5 kV	$5.64 \times 10^{-3}$	$6.52 \times 10^{-2}$	$1.18 \times 10^{+0}$	$3.25 \times 10^{-3}$	$1.19 \times 10^{-6}$	16.64	–	–
	10 kV	$7.61 \times 10^{-3}$	$7.21 \times 10^{-2}$	$1.59 \times 10^{+0}$	$3.25 \times 10^{-3}$	$1.78 \times 10^{-6}$	17.49	–	–
	15 kV	$9.47 \times 10^{-3}$	$7.75 \times 10^{-2}$	$1.98 \times 10^{+0}$	$3.25 \times 10^{-3}$	$2.38 \times 10^{-6}$	18.14	–	–
	20 kV	$1.55 \times 10^{-2}$	$9.13 \times 10^{-2}$	$3.23 \times 10^{+0}$	$3.25 \times 10^{-3}$	$4.59 \times 10^{-6}$	19.68	–	–
	25 kV	$2.20 \times 10^{-2}$	$1.03 \times 10^{-1}$	$4.60 \times 10^{+0}$	$3.25 \times 10^{-3}$	$7.35 \times 10^{-6}$	20.88	–	–
	30 kV	$7.16 \times 10^{-2}$	$1.52 \times 10^{-1}$	$1.50 \times 10^{+1}$	$3.25 \times 10^{-3}$	$3.54 \times 10^{-5}$	25.41	4.23	4.37
PLA in CHCl <sub>3</sub> /THF (1/1) <sup>b</sup>	5 kV	$5.64 \times 10^{-3}$	$5.69 \times 10^{-2}$	$1.18 \times 10^{+0}$	$3.01 \times 10^{-3}$	$9.65 \times 10^{-7}$	19.13	–	–
	10 kV	$7.61 \times 10^{-3}$	$6.29 \times 10^{-2}$	$1.60 \times 10^{+0}$	$3.01 \times 10^{-3}$	$1.44 \times 10^{-6}$	20.11	–	–
	15 kV	$9.47 \times 10^{-3}$	$6.76 \times 10^{-2}$	$1.99 \times 10^{+0}$	$3.01 \times 10^{-3}$	$1.93 \times 10^{-6}$	20.85	–	–
	20 kV	$1.55 \times 10^{-2}$	$7.96 \times 10^{-2}$	$3.25 \times 10^{+0}$	$3.01 \times 10^{-3}$	$3.71 \times 10^{-6}$	22.63	–	–
	25 kV	$2.20 \times 10^{-2}$	$8.96 \times 10^{-2}$	$4.62 \times 10^{+0}$	$3.01 \times 10^{-3}$	$5.94 \times 10^{-6}$	24.00	–	–
	30 kV	$7.16 \times 10^{-2}$	$1.33 \times 10^{-1}$	$1.50 \times 10^{+1}$	$3.01 \times 10^{-3}$	$2.86 \times 10^{-5}$	29.22	2.64	3.30

<sup>a</sup> The PLA products were fabricated at Conc. = 7.27 wt%, FR = 0.25 mL/h, and TCD = 20 cm, with CF = 1800 rpm.<sup>b</sup> The PLA products were fabricated at Conc. = 6.67 wt%, FR = 0.25 mL/h, and TCD = 20 cm, with CF = 1800 rpm.<sup>c</sup> Nanoscale three-point bend test measured by AFM.<sup>d</sup> Elastic-plastic nanoindentation test measured by nanoindenter.**Table 3**

Dimensionless (groups) and mechanical properties of PAN nanofibers fabricated under the different operational conditions.

Sample symbol	Peclet number ( $Pe$ )	Reynolds number ( $Re$ )	Weber number ( $We$ )	Epsilon number ( $\varepsilon$ )	Dimensionless group ( $\Pi_1$ )	Ohnesorge number ( $Oh$ )	Modulus (GPa) <sup>i</sup>	Modulus (GPa) <sup>j</sup>
PAN- <i>b</i> <sup>a</sup>	$2.25 \times 10^{-6}$	$1.18 \times 10^{-2}$	$2.65 \times 10^{-2}$	$5.87 \times 10^{-7}$	$1.56 \times 10^{-14}$	13.83	–	–
PAN- <i>c</i> <sup>b</sup>	$1.80 \times 10^{-5}$	$6.31 \times 10^{-3}$	$5.28 \times 10^{-2}$	$9.31 \times 10^{-6}$	$1.06 \times 10^{-12}$	36.41	–	–
PAN- <i>d</i> <sup>c</sup>	$7.21 \times 10^{-5}$	$3.06 \times 10^{-3}$	$1.07 \times 10^{-1}$	$3.72 \times 10^{-5}$	$8.21 \times 10^{-12}$	106.86	–	–
PAN- <i>d</i> <sub>1</sub> <sup>d</sup>	$2.29 \times 10^{-4}$	$4.50 \times 10^{-3}$	$3.40 \times 10^{-1}$	$3.72 \times 10^{-5}$	$3.84 \times 10^{-11}$	129.59	–	–
PAN- <i>d</i> <sub>2</sub> <sup>e</sup>	$4.11 \times 10^{-4}$	$5.46 \times 10^{-3}$	$6.08 \times 10^{-1}$	$3.72 \times 10^{-5}$	$8.35 \times 10^{-11}$	142.80	–	–
PAN- <i>d</i> <sub>3</sub> <sup>f</sup>	$8.47 \times 10^{-4}$	$6.95 \times 10^{-3}$	$1.25 \times 10^{+0}$	$3.72 \times 10^{-5}$	$2.19 \times 10^{-10}$	161.10	0.54	1.46
PAN- <i>d</i> <sub>4</sub> <sup>g</sup>	$2.20 \times 10^{-3}$	$9.56 \times 10^{-3}$	$3.26 \times 10^{+0}$	$3.72 \times 10^{-5}$	$7.83 \times 10^{-10}$	188.90	1.30	3.68
PAN- <i>d</i> <sub>5</sub> <sup>h</sup>	$9.02 \times 10^{-3}$	$1.53 \times 10^{-2}$	$1.33 \times 10^{+1}$	$3.72 \times 10^{-5}$	$5.13 \times 10^{-9}$	238.94	6.29	4.55

<sup>a</sup> The PAN products were fabricated at Conc. = 8 wt%, FR = 1.0 mL/h, TCD = 10 cm, and EF = 10 kV, with CF = 1800 rpm.<sup>b</sup> The PAN products were fabricated at Conc. = 10 wt%, FR = 1.0 mL/h, TCD = 10 cm, and EF = 10 kV, with CF = 1800 rpm.<sup>c</sup> The PAN products were fabricated at Conc. = 12 wt%, FR = 1.0 mL/h, TCD = 10 cm, and EF = 10 kV, with CF = 1800 rpm.<sup>d</sup> The PAN products were fabricated at Conc. = 12 wt%, FR = 0.5 mL/h, TCD = 10 cm, and EF = 10 kV, with CF = 1800 rpm.<sup>e</sup> The PAN products were fabricated at Conc. = 12 wt%, FR = 0.25 mL/h, TCD = 10 cm, and EF = 10 kV, with CF = 1800 rpm.<sup>f</sup> The PAN products were fabricated at Conc. = 12 wt%, FR = 0.25 mL/h, TCD = 20 cm, and EF = 10 kV, with CF = 1800 rpm.<sup>g</sup> The PAN products were fabricated at Conc. = 12 wt%, FR = 0.25 mL/h, TCD = 20 cm, and EF = 20 kV, with CF = 1800 rpm.<sup>h</sup> The PAN products were fabricated at Conc. = 12 wt%, FR = 0.25 mL/h, TCD = 20 cm, and EF = 30 kV, with CF = 1800 rpm.<sup>i</sup> Nanoscale three-point bend test measured by AFM.<sup>j</sup> Elastic-plastic nanoindentation test measured by nanoindenter.

is in the sub-nanometer range. A schematic diagram of the elastic-plastic nanoindentation test and AFM-scanned cross-sectional profiles were provided in our previous study [38].

#### 2.4. The definition of dimensionless groups

The dimensionless parameters in electrospinning can be divided into the following three categories: operation parameters ( $Q$ ,  $I$ , and  $E$ ), geometric parameters ( $R_0$  and  $L$ ), and materials parameters ( $\rho$ ,  $\eta_0$ ,  $K$ ,  $\gamma$ ,  $\varepsilon$ , and  $\bar{\varepsilon}$ ) [35]. Among these parameters,  $Q$  is the constant volume flow rate,  $I$  is the constant total current in the jet, and  $E$  is the  $z$  component of the electric field. The  $R_0$  is the radius at the origin of an electrically charged viscoelastic jet immediately outside the nozzle, and  $L$  is the entire length of the fiber. The  $\rho$ ,  $\eta_0$ ,  $K$ , and  $\gamma$  are the density, zero-shear-rate viscosity, conductivity, and surface tension of the liquid, respectively, while  $\varepsilon$  and  $\bar{\varepsilon}$  are the dielectric constants of the jet and the ambient air, respectively. The velocity ( $v_0$ ), electric field ( $E_0$ ), and surface charge density ( $\sigma_0$ ) were calculated from the operation, geometric, and materials parameters. The dimensionless groups ( $Pe$ ,  $Re$ ,  $We$ , and  $\varepsilon$  numbers) were then calculated from the characteristic quantities,  $v_0$ ,  $E_0$ , and

$\sigma_0$ , as previously mentioned [35]. The Peclet ( $Pe$ ) number is a ratio of charge convection to conduction, the Reynolds ( $Re$ ) number is a ratio of inertial to viscous stresses, the Weber ( $We$ ) number is a ratio of inertial to surface stresses, and the Epsilon ( $\varepsilon$ ) number is a ratio of electrostatic to inertial stresses [35,36]. The dimensionless surface stress, also called the Ohnesorge ( $Oh$ ) number, were derived from the dimensionless groups mention above ( $We$  and  $Re$  numbers); the dimensionless viscous stress ( $\Pi_1$ ), can be interpreted as a dimensionless stress driving jet elongation, were derived from the dimensionless groups mention above ( $Pe$ ,  $Re$ , and  $\varepsilon$  numbers) [36]; and the results are shown in Tables 1–3.

### 3. Results and discussion

#### 3.1. Effect on a viscoelastic jet

To clearly understand the differences between electrospinning and electrospinning/forcespinning, this study used the dimensionless numbers ( $Pe$ ,  $Re$ ,  $We$ , and  $\varepsilon$  numbers) and dimensionless groups ( $\Pi_1$  and  $Oh$  numbers) to deeply analyze the behavior of a viscoelastic jet. For the conventional electrospinning technique,

electrostatic force is a key factor for driving jet acceleration. It is noteworthy that for the novel electrospinning technique, centrifugal force is a key factor in enhancing jet velocity ( $v_0$ ) and optimizing jet behavior (e.g., inertial stress, electrical convection, and viscous stress). Thus, when a fluid was subjected to the effects of linear velocity or angular velocity in a pipeline, the dimensionless numbers and dimensionless groups were completely different. Here, an  $Re$  number was selected to conduct the formula derivation, and the electrostatic force was not considered in the dimensionless analysis.

In a dimensionless analysis, certain dimensions must be established as fundamental dimensions, so that all of the other dimensions can be expressed in terms of those dimensions. One of these fundamental dimensions is length, symbolized by  $L$ . Thus, area and volume may be expressed in terms of the functional dimension as  $L^2$  and  $L^3$ , respectively. A second fundamental dimension is time, symbolized by  $t$ . The kinematic quantities, velocity and acceleration, may be expressed as  $L/t$  and  $L/t^2$ , respectively. An-

other term that possesses a fundamental dimension is mass, symbolized by  $M$ . An example of a quantity whose dimensional expression involves mass is density, which would be expressed as  $M/L^3$ . Newton's Second Law of Motion gives a relation between force and mass; using this relation force can be expressed in terms of functional dimensions as

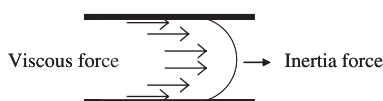
$$F = Ma = M \frac{L}{t^2}$$

If the differential equation describing a given flow situation is known, then dimensional homogeneity requires that each term in the equation have the same units. The ratio of one term in the equation to another must then be dimensionless. A classic example of this type of analysis involves the use of the Navier–Stokes equation in the following form:

$$\frac{Dv}{Dt} = g - \frac{\nabla P}{\rho} + \nu \nabla^2 v \quad (1)$$

### Linear velocity

Step 1



$$Re = \frac{\text{Inertia force}}{\text{Viscous force}} = \frac{L \cdot u}{\nu}$$

Step 2

Variable	Symbol	Dimension
velocity	$v$	$L / t$
density	$\rho$	$M / L^3$
length	$L$	$L$
viscosity	$\mu$	$M / Lt$
force	$F$	$ML / t^2$

Step 3

$$\text{For } M, \quad 0 = b + 1 \quad \rightarrow \quad b = -1$$

$$\text{For } L, \quad 0 = a - 3b + c - 1 \quad \rightarrow \quad c = -1$$

$$\text{For } t, \quad 0 = -a - 1 \quad \rightarrow \quad a = -1$$

$$Re = \frac{\text{Inertia force}}{\text{Viscous force}} = \frac{\rho \cdot u \cdot L}{\mu}$$

### Angular velocity

Step 4



$$Re = \frac{\text{Inertia force}}{\text{Viscous force}} = \frac{L \cdot u_a}{\nu}$$

Step 5

Variable	Symbol	Dimension
angular velocity	$v_a$	$1 / t$
density	$\rho$	$M / L^3$
length	$L$	$L$
viscosity	$\mu$	$M / Lt$
force	$F$	$ML / t^2$

Step 6

$$\text{For } M, \quad 0 = b + 1 \quad \rightarrow \quad b = -1$$

$$\text{For } L, \quad 0 = -3b + c - 1 \quad \rightarrow \quad c = -2$$

$$\text{For } t, \quad 0 = -a - 1 \quad \rightarrow \quad a = -1$$

$$Re = \frac{\text{Inertia force}}{\text{Viscous force}} = \frac{\rho \cdot u_a \cdot L^2}{\mu}$$

Fig. 1. Calculation steps of  $Re$  number for a viscoelastic jet under the driven of linear velocity or angular velocity.



Each term in this expression can be expressed by a variable or combination of variables. Each term also has a physical significance, so the ratio of any two of them will produce a dimensionless group. Dividing each of the terms on the right-hand side of Eq. (1) by the inertial forces, the dimensionless parameters will be formed, including the Reynolds ( $Re$ ) number (see Step 1 of Fig. 1). To determine the dimensionless groups from the variables involved in the flow of fluid to a solid body, the force exerted on the body is a function of velocity ( $v$ ), density ( $\rho$ ), viscosity ( $\mu$ ), and length ( $L$ ). The usual first step is to construct a table of the variables and their dimensions (see Step 2 of Fig. 1). The two dimensionless parameters will be symbolized with  $\pi_1$  and  $\pi_2$ , and may be formed in several ways. We now know that  $\pi_1$  and  $\pi_2$  both include  $\rho$ ,  $L$ , and  $v$ , that one of them includes  $F$  and the other  $\mu$ , and that they are both dimensionless. For each to be dimensionless, the variables must be raised to certain exponents. Considering each group independently,  $\pi_1 = v^a \rho^b L^c \mu$  were formed (here,  $\pi_2$  is not considered in the dimensionless analysis) dimensionally. The  $M$ ,  $L$ , and  $t$  exponents were equalized on both sides of this expression; thus, our first dimensionless group is displayed in Step 3 of Fig. 1.

When the linear velocity is changed into an angular velocity, dividing each of the terms on the right-hand side of Eq. (1) by the inertial forces will form the dimensionless parameters, including the Reynolds ( $Re$ ) number (see Step 4 of Fig. 1). To determine the dimensionless groups from the variables involved in the flow of fluid to a solid body, the force exerted on the body can be expressed as a function of  $v$ ,  $\rho$ ,  $\mu$ , and  $L$ . The usual first step is to construct a table of the variables and their dimensions (see Step 5 of Fig. 1). Considering each group independently,  $\pi_1 = v^a \rho^b L^c \mu$  were formed (here,  $\pi_2$  is not considered in the dimensionless analysis) dimensionally. The exponents  $M$ ,  $L$ , and  $t$  were equalized on both sides of this expression, as shown in Step 6 of Fig. 1. From the above results, it was determined that the  $L$  of the  $Re$  number will become the  $L^2$  of  $Re$  number when the linear velocity is changed into the angular velocity. The  $L$  is expressed as a traveled length of the fluid [52]. It can be determined that the traveled length of the fluid ( $L$ ) will double during the formula derivation steps (see Steps 1–6 of Fig. 1). The square of the traveled length of the fluid, ( $L^2$ ), will help to reduce the jet radius ( $R_0$ ) and further enhance the jet velocity ( $v_0$ ). The specific behavior of an electrically charged, rotating viscoelastic jet will be able to improve the problems of the current electrospinning technique.

Furthermore, the novel electrospinning technique has a stronger stretching force and a faster extension speed than the conventional electrospinning technique. The schematic exhibited in Fig. 2 shows the differences between the conventional and novel electrospinning techniques. The conventional electrospinning technique only has a stretching force in the axial ( $\vec{a}_x$ ) direction under an electrostatic field. It is noteworthy that the novel electrospinning technique has a stretching force in the axial ( $\vec{a}_y$ ) and tangential ( $\vec{a}_x$ ) directions under electrostatic and centrifugal fields (see Fig. 2). It can be found that a viscoelastic jet will also have the driving forces of instantaneous velocity ( $v = r \times \omega = 15.08$  m/s) and tangential acceleration ( $a_c = \sqrt{a_x^2 + a_y^2} = r \times \omega^2 = 2.84 \times 10^3$  m/s<sup>2</sup>) [53] with more than a stretching force in the tangential direction. The instantaneous velocity ( $v$ ) and tangential acceleration ( $a_c$ ) do not appear in the conventional electrospinning technique [13–21,32–34]. Moreover, the CCD images demonstrate the variations of the Taylor cone and jet under the electrostatic force and the electrostatic/centrifugal forces. From previous studies, it was found that in every electrospinning technique [13–21,32–34], the “whipping instability” still existed. It is noteworthy that the combination of electrospinning and forcespinning is able to impose a strong stretching force and a fast extension speed on a viscoelastic jet, which further removes the whipping instability. In addition, the jet radius ( $R_0$ ) can be measured by CCD images and calculated in the velocity ( $v_0 = Q/\pi R_0^2$ ).

To observe the differences in the jet radius ( $R_0$ ) and the velocity ( $v_0 = Q/\pi R_0^2$ ) of a viscoelastic jet, a 14 wt% PC/THF solution was used to conduct the electrospinning and electrospinning/forcespinning experiments under the same operational conditions (FR = 0.25 mL/h, WD = 20 cm, EF = 25 kV,  $T = 25$  °C, and CF = 1,800 rpm). The jet radius is 0.130 and 0.028 cm for a viscoelastic PC jet under an electrostatic field and electrostatic/centrifugal field, respectively. It is noteworthy that the velocity ( $v_0$ ) is 4.71 and  $1.02 \times 10^2$  mL/h cm<sup>2</sup> for a viscoelastic PC jet. The velocity ( $v_0 = 1.02 \times 10^2$  mL/h cm<sup>2</sup>) of an electrically charged, rotating viscoelastic PC jet is much higher than the velocity ( $v_0 = 4.71$  mL/h cm<sup>2</sup>) of an electrically charged viscoelastic PC jet. In addition, the 6.7 wt% PLA/CHCl<sub>3</sub>/THF and 12 wt% PAN/DMF solutions were used to conduct the electrospinning and electrospinning/forcespinning experiments under the same operational conditions (FR = 0.25 mL/h, WD = 20 cm, EF = 25 kV, and

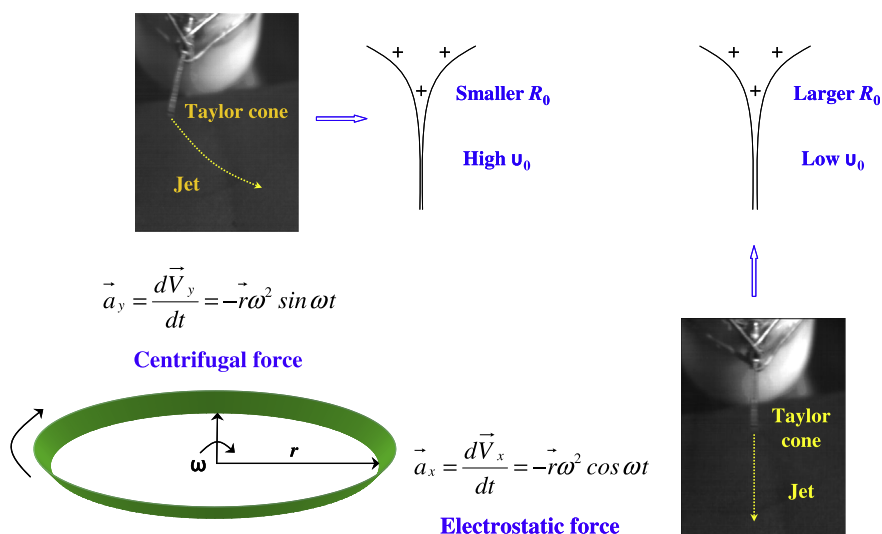


Fig. 2. Schematic diagram and CCD images show the differences of jet radius ( $R_0$ ) and velocity ( $v_0$ ) under the driven of electrospinning (stretching force from axial direction) and electrospinning/forcespinning (stretching force from axial and tangent directions).

CF = 1,800 rpm). The velocity ( $v_0 = 1.09 \times 10^2$  mL/h cm<sup>2</sup> for a PLA jet and  $v_0 = 1.27 \times 10^2$  mL/h cm<sup>2</sup> for a PAN jet) of an electrically charged rotating viscoelastic jet is much higher than the velocity ( $v_0 = 5.09$  mL/h cm<sup>2</sup> for a PLA jet or  $v_0 = 3.18 \times 10^1$  mL/h cm<sup>2</sup> for a PAN jet) of an electrically charged viscoelastic jet. It can be determined that a high velocity ( $v_0$ ) can successfully create a strong stretching force and a fast extension speed that can be imposed onto a viscoelastic jet. This result demonstrates that an additional centrifugal field can improve the motor behavior (e.g., jet radius, velocity, inertial stress, electrical convection, and viscous stress) of a viscoelastic jet.

To deeply analyze the jet behavior, Fig. 3 shows the variations of an electrically charged rotating viscoelastic jet at each stage through the calculation of dimensionless numbers ( $Pe$ ,  $Re$ ,  $We$ , and  $\varepsilon$  numbers) and dimensionless groups ( $\Pi_1$  and  $Oh$  numbers). First, the  $Re$  number is a ratio of inertial to viscous stresses, representing the kinetic energy of the jet relative to viscous dissipation [36]. The viscosity and velocity are obtained from the average momentum of numerous molecules for a viscoelastic fluid. For a near-laminar flow fluid, the entropy and movement frequency of numerous molecules decreased due to the viscosity dominance. For a near-turbulent flow fluid, the entropy and movement frequency of numerous molecules increased due to the velocity dominance. Părău et al. [54] stated that the radius of curvature of a viscous fluid jet becomes more tightly coiled as viscosity increases (smaller  $Re$  number). A viscous fluid jet resulted in a centerline with a large radius of curvature as the viscosity decreases (larger  $Re$  number). The jet radius will gradually thin when the radius of curvature increases (larger  $Re$  number). In addition, the  $We$  number is a ratio of inertial to surface stresses representing the kinetic energy of the jet relative to tension dissipation [36]. Similarly, Părău et al. [54] stated that the radius of curvature of a viscous fluid jet becomes more tightly coiled as the surface tension increases (smaller  $We$  number). A viscous fluid jet resulted in a

centerline with a large radius of curvature as the surface tension decreases (larger  $We$  number). The jet radius will gradually thin as the radius of curvature increases (larger  $We$  number). Thus, the magnitude of the radius of curvature for an electrically charged, rotating viscoelastic jet can be obtained by the  $Re$  and  $We$  numbers, as exhibited in Fig. 3.

The  $Pe$  number is a ratio of electrical convection to conduction, representing the motion of free charges relative to the jet motion [36]. The positive charges accumulate around the needle as electrical conduction increases (smaller  $Pe$  number); moreover, only a smaller amount of positive charge exists in a liquid droplet. Thus, when a viscoelastic jet wants to break the liquid droplet, the jet cannot continuously thin because the amount of positive charge in the liquid droplet is insufficient. The positive charge accumulates in a liquid droplet as the electrical convection increases (larger  $Pe$  number). A viscoelastic jet has enough positive charge to break the liquid droplet and produce continuous thinning. Rutledge and Fridrikh [55] stated that a viscous fluid jet resulted in a shorter jet length as electrical conduction increased (smaller  $Pe$  number). Furthermore, the perturbation phenomenon becomes more violent in a stable jet due to the non-uniform positive charge distribution in a viscoelastic jet (smaller  $Pe$  number) [55]. A viscous fluid jet results in a longer jet length as electrical convection increases (larger  $Pe$  number). A stable jet will be formed because the positive charge is uniformly distributed in a viscoelastic jet (larger  $Pe$  number). The jet radius will gradually thin as the jet length increases. In addition, the  $\varepsilon$  number is the ratio of electrostatic to inertial stresses [35,36]. A viscoelastic jet is simultaneously affected by the electrostatic force and the gravitational force during the electrospinning process. A viscoelastic jet does not have enough time to carry out jet thinning when the gravitational force is greater than the electrostatic force (smaller  $\varepsilon$  number), and the length of the viscoelastic jet becomes shorter. A viscoelastic jet has enough time to carry out jet thinning when

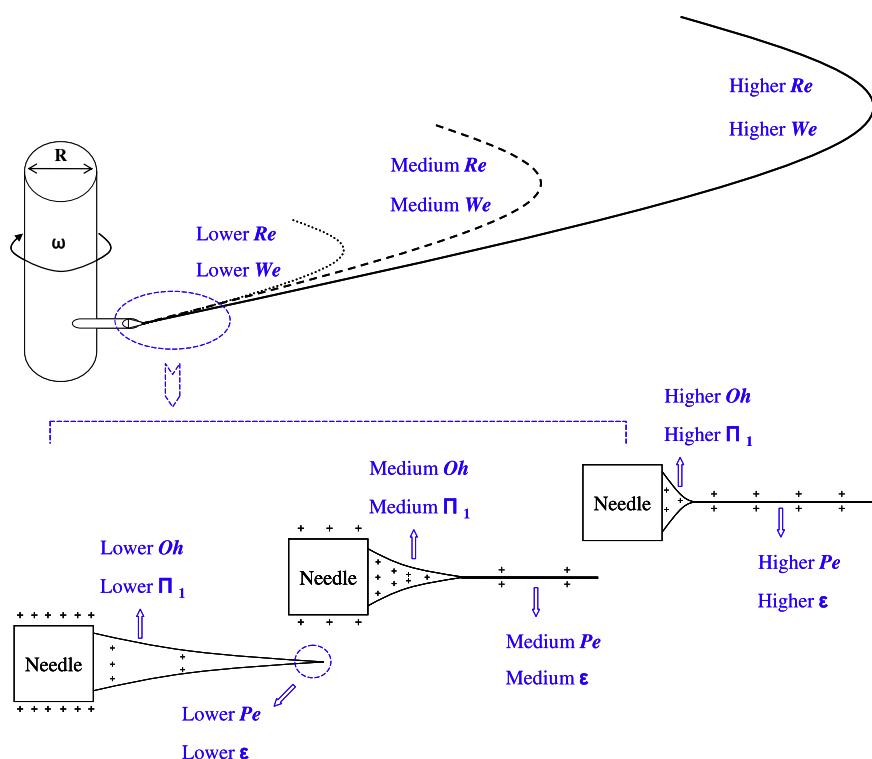


Fig. 3. Schematic diagram shows the variations of curvature radius (by  $Re$  and  $We$  numbers), jet length (by  $Pe$  and  $\varepsilon$  numbers), and Taylor cone (by  $\Pi_1$  and  $Oh$  numbers) for an electrically charged rotating viscoelastic jet.

the electrostatic force is greater than the gravitational force (larger  $\varepsilon$  number), and the length of a viscoelastic jet becomes longer. This result is consistent with the  $Pe$  number. Thus, the variation in jet length for an electrically charged, rotating viscoelastic jet can be determined by the  $Pe$  and  $\varepsilon$  numbers, as displayed in Fig. 3.

The  $Oh$  number is a ratio of viscous to surface stresses. The  $Oh$  number is known to describe the behavior of free surface flows in which small disturbances lead to the capillary breakup of a jet of fluid [36]. When the  $Oh$  number decreases, viscous forces within the jet are insufficient to stabilize the disturbances, leading to capillary breakup. As the  $Oh$  number increases, viscous forces stabilize the disturbances at the jet surface, leading to a beads-on-a-string configuration at intermediate  $Oh$  values and stable jets at sufficiently high  $Oh$  values [36]. The  $\Pi_1$  number is the ratio of electrostatic to electroviscous stresses experienced by an electrostatically driven fluid jet and can be interpreted as a dimensionless stress that drives jet elongation [36]. When  $\Pi_1$  increases under a constant  $Oh$  number, the viscous forces within the jet are insufficient to stabilize the disturbances, leading to capillary breakup. As  $\Pi_1$  decreases under a constant  $Oh$  number, the viscous forces stabilize the disturbances at the jet surface, leading to a beads-on-a-string configuration at intermediate  $Oh$  numbers and stable jets at sufficiently high  $Oh$  numbers [36]. Thus, the morphology of the Taylor cone for an electrically charged, rotating viscoelastic jet can be predicted by  $\Pi_1$  and the  $Oh$  numbers, as revealed in Fig. 3. From the above discussion, it is clear that the radius of curvature, jet length, and Taylor cone for an electrically charged, rotating viscoelastic jet can be described by the  $Re$  and  $We$ ,  $Pe$  and  $\varepsilon$ ,  $\Pi_1$  and  $Oh$  numbers (see Fig. 3).

### 3.2. The relationship of jet behavior and product morphology

To further optimize the behavior of an electrically charged, rotating viscoelastic jet, an  $Re$  number was selected to explore the relationship between jet behavior (e.g., radius of curvature, jet length, and the Taylor cone) and product morphology (e.g., beads, beaded fibers, and nanofibers), as revealed in Fig. 4. Electrostatic fields (5, 10, 15, 20, 25, and 30 kV) and temperatures (25, 30, 35, 40, and 45 °C) were selected to execute the electrospinning/forcespinning experiments under a 14 wt% PC/THF solution with a flow rate of 0.25 mL/h, a spinneret tip-to-collector distance of 20 cm, and an additional centrifugal field of 1800 rpm for inducing the anisotropic structural property in PC nanofibers [38]. A viscoelastic jet only has a smaller  $Re$  number ( $Re = 4.17 \times 10^{-2}$ ) under a lower electrostatic field (5 kV), as displayed in Table 1. From the above explanation, it is clear that a viscoelastic jet resulted in a centerline with a small radius of curvature due to a smaller  $Re$  number. When the electrostatic field gradually increased to 15 or 25 kV, the  $Re$  number increased ( $Re = 5.15 \times 10^{-2}$  or  $9.38 \times 10^{-2}$  for 15 or 25 kV, respectively), and a viscoelastic jet resulted with a centerline with a radius of curvature due to the larger  $Re$  number. Thus, a viscoelastic jet does not have enough time to thin when the radius of curvature is smaller. A larger radius of curvature can ensure that the jet has enough time to thin. To clearly observe the relation between jet behavior and product morphology, the plot of  $Re$  number vs. average diameter (nm) of PC nanofibers is shown in Fig. 4. The product morphology tends to be beaded fibers (1484 nm) under a lower electrostatic field (5 kV) due to a smaller radius of curvature. The diameter of the beaded fibers decreased (526 nm) when the electrostatic field was increased to 15 kV. The uniaxially aligned PC nanofibers (270 nm) can be successfully fabricated under the higher electrostatic field (25 kV) due to a larger radius of curvature (see Table 1, Figs. 3 and 4). From the above explanation, an additional centrifugal field (1800 rpm) combined with a higher electrostatic field (25 kV) can produce a stronger stretching force, and a viscoelastic jet will be able to continue

thinning and further form the uniaxially aligned PC nanofibers due to this unique stretching force. Otherwise, a weak stretching force will result when a lower electrostatic field (5 kV) is applied with a centrifugal field, and the beaded fibers will appear on the copper ring of the collector. The product morphology (e.g., beads, beaded fibers, and nanofibers) is clearly distinguished by two dividing lines determined from the  $Re$  number (see Table 1 and Fig. 4). According to the above results, nanofibers, beaded fibers, or beads will be obtained when the  $Re$  number is higher than  $6.57 \times 10^{-2}$ , between  $2.77 \times 10^{-2}$  and  $6.57 \times 10^{-2}$ , or lower than  $2.77 \times 10^{-2}$ , respectively (see Table 1 and Fig. 4). Thus, this study was successful in building an innovative model to determine the product morphology of PC through the calculation of the  $Re$  number or other dimensionless groups.

To induce anisotropic structural properties in PLA nanofibers, solutions of 7.27 wt% PLA/CH<sub>2</sub>Cl<sub>2</sub>/DMF and 6.67 wt% PLA/CHCl<sub>3</sub>/DMF and electrostatic fields of 5, 10, 15, 20, 25, and 30 kV were selected to execute the electrospinning/forcespinning experiments, with a flow rate of 0.25 mL/h, a spinneret tip-to-collector distance of 20 cm, and an additional centrifugal field of 1800 rpm [39]. A viscoelastic jet has a smaller radius of curvature ( $Re = 6.52 \times 10^{-2}$  or  $5.69 \times 10^{-2}$  for CH<sub>2</sub>Cl<sub>2</sub> or CHCl<sub>3</sub>) under a lower electrostatic field (5 kV). The beaded fibers were formed when the jet had a smaller

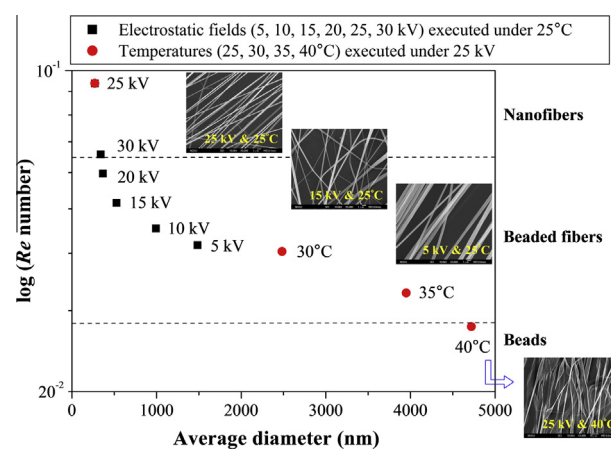


Fig. 4. Plot of  $Re$  number vs. average diameter (nm) of PC nanofibers (The dash line is dividing line indicated the relationship of inertial stress/viscous stress and product morphology).

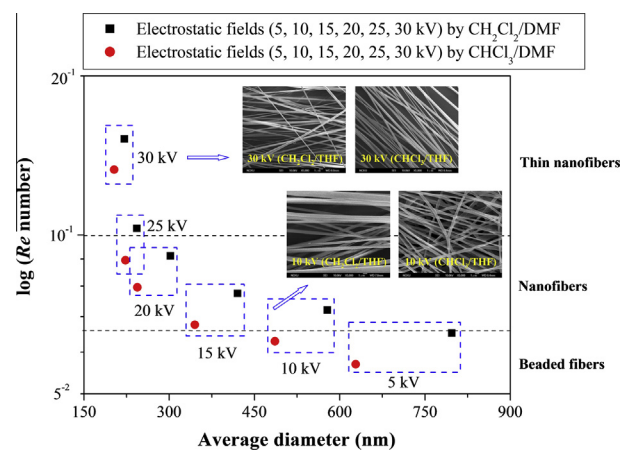


Fig. 5. Plot of  $Re$  number vs. average diameter (nm) of PLA nanofibers (The dash line is dividing line indicated the relationship of inertial stress/viscous stress and product morphology).



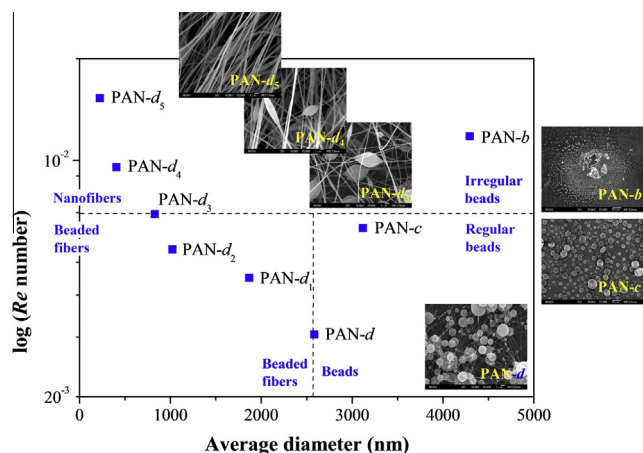


Fig. 6. Plot of  $Re$  number vs. average diameter (nm) of PAN nanofibers (The dash line is dividing line indicated the relationship of viscous stress, surface tension, inertial stress and product morphology).

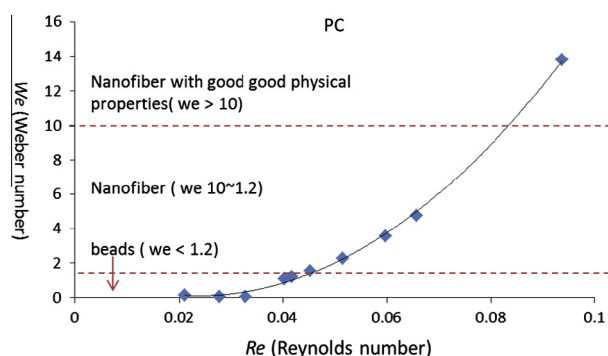


Fig. 7. Plot of  $Re$  number vs.  $We$  number of PC nanofibers (The dash line is dividing line indicated the relationship of viscous stress, surface tension, inertial stress and product morphology).

radius of curvature (smaller  $Re$  number) [54], as shown in Table 2 and Fig. 5. When the electrostatic field increases to 10 kV, the radius of curvature will gradually become larger ( $Re = 7.21 \times 10^{-2}$  or  $6.29 \times 10^{-2}$  for  $\text{CH}_2\text{Cl}_2$  or  $\text{CHCl}_3$ ). The diameters of the PLA nanofibers fabricated using 7.27 wt% PLA/ $\text{CH}_2\text{Cl}_2$ /DMF and 6.67 wt% PLA/ $\text{CHCl}_3$ /DMF are 578 and 486 nm, respectively. When an additional centrifugal field (1800 rpm) was combined with a high electrostatic field (30 kV), the viscoelastic jet possessed a centerline with the largest radius of curvature ( $Re = 1.52 \times 10^{-1}$  or

$1.33 \times 10^{-1}$  for  $\text{CH}_2\text{Cl}_2$  or  $\text{CHCl}_3$ ). The diameters of the PLA nanofibers fabricated using 7.27 wt% PLA/ $\text{CH}_2\text{Cl}_2$ /DMF and 6.67 wt% PLA/ $\text{CHCl}_3$ /DMF were 221 and 203 nm, respectively. Furthermore, the resulting PLA nanofibers will also be uniaxially aligned (see Fig. 5). According to above results, thin nanofibers, nanofibers, or beaded fibers will be obtained when the  $Re$  number is larger than  $8.96 \times 10^{-2}$ , between  $6.76 \times 10^{-2}$  and  $8.96 \times 10^{-2}$ , or lower than  $6.76 \times 10^{-2}$ , respectively. The product morphology (e.g., beaded fibers, nanofibers, and thin nanofibers) can be clearly observed by the two dividing lines calculated from the  $Re$  number (see Fig. 5 and Table 2). This study was successful in building an innovative model to determine the product morphology of PLA through the calculation of the  $Re$  number or other dimensionless groups.

To further examine the anisotropic structural properties of PAN nanofibers, PAN/DMF ratios of 6, 8, 10, 12, and 14 wt%, flow rates of 0.25, 0.5, and 1.0 mL/h, spinneret tip-to-collector distances of 10 and 20 cm, and electrostatic fields of 10, 20, and 30 kV were studied under an additional centrifugal field (1800 rpm). It is noteworthy that the PAN-b (8 wt% PAN/DMF ratio) has a higher  $Re$  number ( $Re = 1.18 \times 10^{-2}$ ), as displayed in Fig. 6 and Table 3. The  $Re$  number is the ratio of inertial to viscous stresses, and it will increase as the velocity dominates over the viscosity. However, irregular beads will also form using the 8 wt% PAN/DMF ratio due to a lack of chain entanglement. The PAN-d (12 wt% PAN/DMF ratio) has a lower  $Re$  number ( $Re = 3.06 \times 10^{-3}$ ) because the  $Re$  number will decrease as the viscosity dominates over the velocity. Regular beads and beaded nanofibers were obtained when the PAN/DMF ratio increased to 10 and 12 wt%, respectively. In addition, the PAN-d<sub>5</sub> (12 wt% PAN/DMF ratio) has the highest  $Re$  number ( $Re = 1.53 \times 10^{-2}$ ). The  $Re$  number will increase due to the combination of an additional centrifugal field (1800 rpm) and a large electrostatic field (30 kV). The uniaxially aligned PAN nanofibers were successfully fabricated after optimizing a series of operational conditions (Conc. = 12 wt%, FR = 0.25 mL/h, TCD = 20 cm, and EF = 30 kV under CF = 1800 rpm) [40]. The product morphology (e.g., irregular beads, regular beads, beaded fibers, and nanofibers) was clearly observed by two dividing lines calculated from the  $Re$  number (see Fig. 6 and Table 3). Furthermore, this innovative model will be able to be applied in the fabrication of a series of polymeric nanofibers in the future. On the other hand,  $Re$  number vs.  $We$  number curve of PC, PLA and PAN was drawn and shown in Figs. 7–9, because the jet morphology was dominated by viscosity ( $Re$ ) and surface tension ( $We$ ) of solution according to our previous studies [37–40]. From Figs. 7–9, one can observe when  $We$  number is over than 10, the uniform polymer nanofibers with good physical properties were prepared by the centrifugal electrospinning. In summary, this study successfully created an electrically charged, rotating viscoelastic jet and optimized the jet behavior

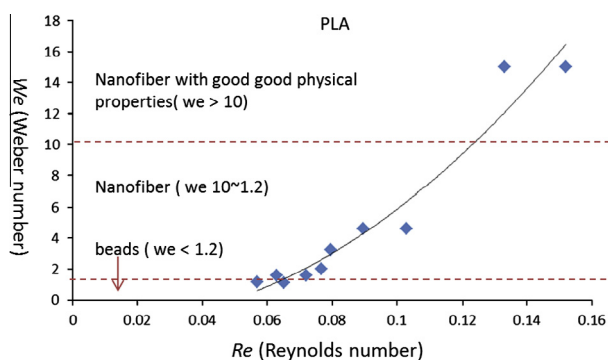


Fig. 8. Plot of  $Re$  number vs.  $We$  number (nm) of PLA nanofibers (The dash line is dividing line indicated the relationship of viscous stress, surface tension, inertial stress and product morphology).

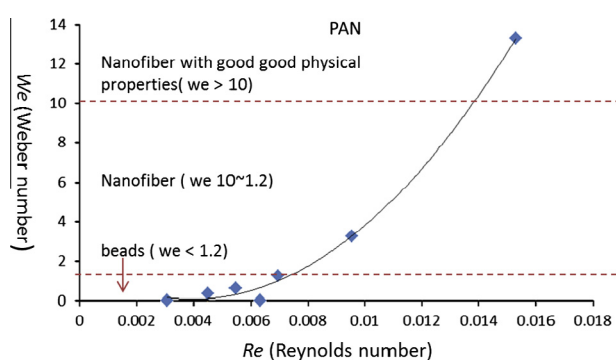
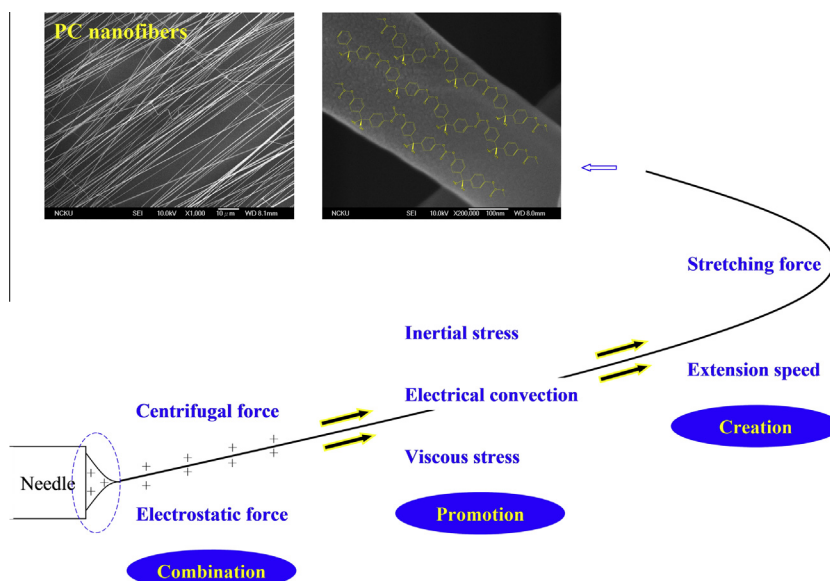


Fig. 9. Plot of  $Re$  number vs.  $We$  number (nm) of PAN nanofibers (The dash line is dividing line indicated the relationship of viscous stress, surface tension, inertial stress and product morphology).



**Fig. 10.** Schematic diagram shows the combination of electrospinning and forcespinning can successfully induce the anisotropic structural properties in polymer nanofibers.

(e.g., curvature radius, jet length, and Taylor cone) to fabricate uniaxially aligned PC, PLA, and PAN nanofibers from the  $Re$  number and other dimensionless groups.

### 3.3. Effect on a single nanofiber

From the above conclusion, it is observed that a viscoelastic jet will simultaneously have the driving force in the axial ( $\vec{a}_x$ ) and tangential ( $\vec{a}_y$ ) directions under electrostatic and centrifugal forces. The combination of the electrostatic and centrifugal forces can successfully produce an electrically charged, rotating viscoelastic jet. Moreover, an electrically charged, rotating viscoelastic jet was simultaneously affected by the inertial stress, electrical convection, and viscous stress. Through the calculation of the  $Re$  and  $We$ ,  $Pe$  and  $\epsilon$ ,  $\Pi_1$  and  $Oh$  numbers, it can be found that a viscoelastic jet will have superior inertial stress, electrical convection, and viscous stress due to a smaller jet radius ( $R_0$ ) and larger velocity ( $v_0$ ) (see Fig. 2). A strong stretching force and a fast extension speed will form after optimizing the inertial stress, electrical convection, and viscous stress. In the past, the anisotropic structural properties in the polymeric nanofiber could not be induced when a “whipping instability” phase existed in the conventional electrospinning technique [13–21,32–34]. It is noteworthy that this strong stretching force and the fast extension speed can effectively remove the phenomenon of “whipping instability”. The stretching force of an electrically charged, rotating viscoelastic jet is superior than the stretching force produced from the conventional electrospinning techniques [2,3,13–21,32–34] (see Fig. 10). A single polymeric nanofiber or nanofiber membrane will have superior physical properties (e.g., conformation, molecular orientation, crystallinity, hardness, and elastic modulus). A schematic, Fig. 10, shows the degree of uniaxial alignment, the ratio of the *trans*–*trans* conformer, and the molecular orientation in the PC nanofibers that were simultaneously enhanced after an induction of a stretching force.

### 3.4. The relationship of jet behavior and physical property

The  $\Pi_1$  number is calculated from the  $Pe$ ,  $Re$ , and  $\epsilon$  numbers, and the  $Oh$  number is calculated from the  $Re$  and  $We$  numbers [36]. The  $\Pi_1$  and  $Oh$  numbers are expressed in the transport in the electrostatic field and the motor behavior of the fluid, respectively [36].

Furthermore, in inducing anisotropic structural properties in the polymeric nanofibers, the dimensionless group  $\Pi_1$  and the  $Oh$  numbers are the key parameters. Thus, this study analyzed the jet behavior (e.g., radius of curvature, jet length, and Taylor cone), product morphology (e.g., beads, beaded fibers, and nanofibers), and physical properties (e.g., conformation, molecular orientation, crystallinity, hardness, and elastic modulus) at each stage of electrospinning/forcespinning. Fig. 11 shows the plot of  $\Pi_1$  and the  $Oh$  numbers vs. average diameter (nm) of the PC nanofibers. It was observed that when  $\Pi_1$  and the  $Oh$  numbers were closer to  $4.39 \times 10^{-6}$  and 33.14, respectively (see Table 1 and Fig. 11), the ratios of the *trans*–*trans* conformer, crystallinity, hardness, and modulus of the PC nanofibers were 61%, 3.0%, 0.32 GPa, and 2.77 GPa, respectively [38]. The anisotropic structural properties in the PC nanofibers can be successfully induced when the transport in the electrostatic field and the motor behavior of the fluid are complementary. Moreover, when  $\Pi_1$  and the  $Oh$  numbers are higher than  $1.83 \times 10^{-5}$  and 39.60, respectively (see Table 1 and Fig. 11), the ratios of the *trans*–*trans* conformer, crystallinity, hardness, and modulus of the PC nanofibers were 67%, 6.5%, 0.52 GPa, and 5.13 GPa, respectively [38]. In addition, the physical properties (e.g., conformation, crystallinity, hardness, and modulus) of the PC nanofibers can be clearly distinguished by the two dividing lines calculated from the  $\Pi_1$  and  $Oh$  numbers (see Table 1 and Fig. 11). Thus, the product morphology and physical properties of the PC nanofibers can be controlled by jet behavior, which is determined from the dimensionless numbers ( $Pe$ ,  $Re$ ,  $We$ , and  $\epsilon$  numbers) and dimensionless groups ( $\Pi_1$  and  $Oh$  numbers).

Fig. 12 presents a plot of the  $\Pi_1$  and  $Oh$  numbers vs. the average diameter (nm) of the PLA nanofibers. It was observed that when  $\Pi_1$  and the  $Oh$  numbers are closer to  $5.94 \times 10^{-6}$  and 24.00, respectively (see Table 2), the ratios of the *tt*(2<sub>1</sub>) helix, dichroic ratio, crystallinity, hardness, and modulus of the PLA nanofibers were 57%, 1.89, 37%, 0.26 GPa, and 3.30 GPa, respectively [39]. Moreover, when  $\Pi_1$  and the  $Oh$  numbers were higher than  $3.54 \times 10^{-5}$  and 25.41, respectively (see Table 2), the ratios of the *tt*(2<sub>1</sub>) helix, dichroic ratio, crystallinity, hardness, and modulus of the PLA nanofibers were 64%, 1.98, 45%, 0.34 GPa, and 4.37 GPa, respectively [39]. The physical properties (e.g., conformation, molecular orientation, crystallinity, hardness, and modulus) of the PLA nanofibers can be clearly distinguished by one dividing line calculated from

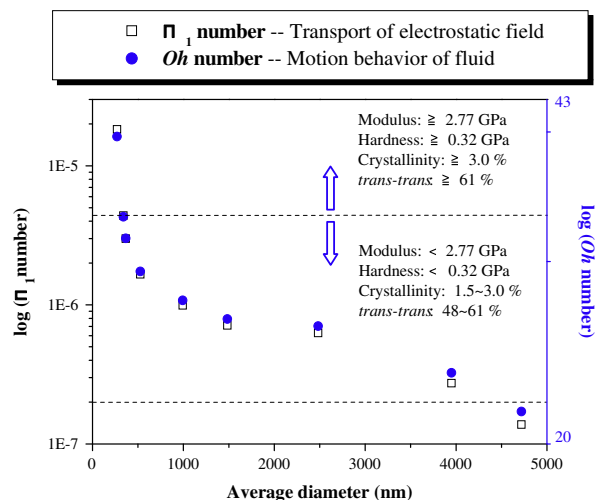


Fig. 11. Plot of  $\Pi_1$  and  $Oh$  numbers vs. average diameter (nm) of PC nanofibers (The dash line is dividing line indicated the relationship of jet behavior and nanofiber conformation).

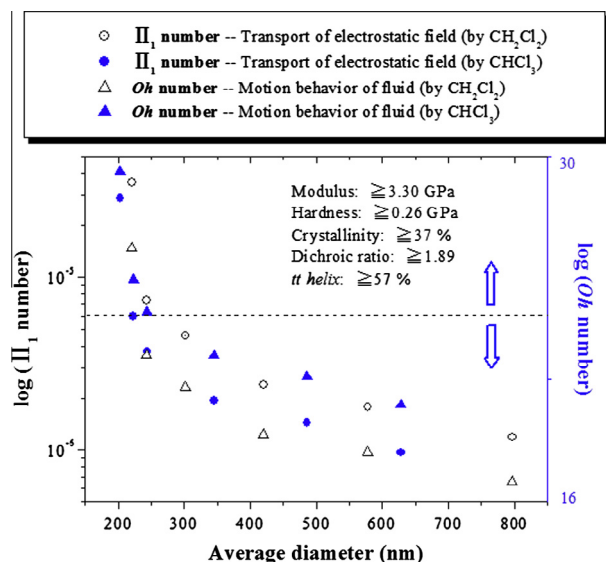


Fig. 12. Plot of  $\Pi_1$  and  $Oh$  numbers vs. average diameter (nm) of PLA nanofibers (The dash line is dividing line indicated the relationship of jet behavior and nanofiber conformation).

the  $\Pi_1$  and the  $Oh$  numbers (see Fig. 12 and Table 2). Fig. 13 shows a plot of  $\Pi_1$  and the  $Oh$  numbers vs. the average diameter (nm) of the PAN nanofibers. It was observed that when  $\Pi_1$  and the  $Oh$  numbers were closer to  $7.83 \times 10^{-10}$  and 188.90, respectively (see Table 3), the dichroic ratio, specific crystallinity, hardness, and modulus of the PAN nanofibers were 0.65, 23%, 0.39 GPa, and 3.68 GPa, respectively [40]. The anisotropic structural properties in the PAN nanofibers can be successfully induced when the transport in the electrostatic field and the motor behavior of the fluid are complementary. Moreover, when  $\Pi_1$  and the  $Oh$  numbers were higher than  $5.13 \times 10^{-9}$  and 238.94, respectively (see Table 3), the dichroic ratio, specific crystallinity, hardness, and modulus of the PAN nanofibers were 0.78, 34%, 0.43 GPa, and 4.55 GPa, respectively. The physical properties (e.g., conformation, crystallinity, hardness, and modulus) of the PAN nanofibers can be clearly distinguished by two dividing lines calculated from the  $\Pi_1$  and  $Oh$  numbers (see Fig. 13 and Table 3). If the dimensionless numbers ( $Re$  number in Figs. 4–6) or dimensionless groups ( $\Pi_1$  are  $Oh$

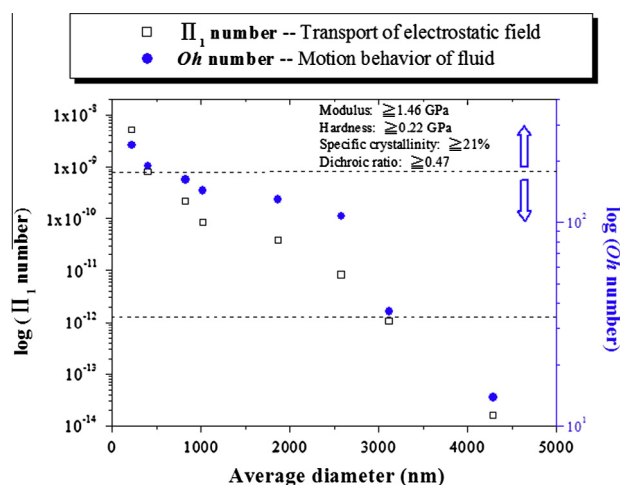


Fig. 13. Plot of  $\Pi_1$  and  $Oh$  numbers vs. average diameter (nm) of PAN nanofibers (The dash line is dividing line indicated the relationship of jet behavior and nanofiber conformation).

numbers in Figs. 8–10) are altered, the jet behavior will affect the product morphology and physical properties. These results demonstrate that the combination of electrospinning and forcesspinning can successfully induce anisotropic structural properties in a series of polymeric nanofibers. Furthermore, this study was also successful in developing an innovative model to predict and fabricate a series of functional polymeric nanofibers. This innovative model for predicting the product morphology and physical properties, the novel electrospinning technique, and the resulting functional polymeric nanofibers will constitute a major milestone in the areas of nanoscience and nanotechnology.

#### 4. Conclusions

A novel electrospinning technique for improving upon the problems of the current electrospinning technique was successfully developed in this study. The combination of electrospinning and forcesspinning can effectively control the jet behavior to create a strong stretching force and a fast extension speed for removing “whipping instability” and prepared the good physical properties and uniaxially aligned of polymer nanofiber. Through dimensionless number and group analysis, higher  $Re(PC = 9.38 \times 10^{-2}$ ,  $PLA = 1.52 \times 10^{-1}$  and  $PAN = 1.53 \times 10^{-2}$ ) and  $We(PLA = 13.8$ ,  $PLA = 15$  and  $PAN = 13.3)$  number of all three systems can collect the bead-free and uniform nanofibers. Similarly, higher  $\Pi_1$  ( $PC = 1.83 \times 10^{-5}$ ,  $PLA = 2.86 \times 10^{-5}$  and  $PAN = 5.13 \times 10^{-9}$ ) and  $Oh(PLA = 39.60$ ,  $PLA = 29.22$  and  $PAN = 238.94)$  numbers refer to viscosity and electrostatic force dominate the jet behavior and obtained the nanofiber with high modulus, hardness, crystallinity and good molecular orientation. Hence, the uniaxially aligned polycarbonate, polylactic acid and polyacrylonitrile nanofibers with superior physical properties (modulus  $\geq 2.77$  GPa, 3.3 GPa and 1.46 GPa, hardness  $\geq 0.32$ , 0.26 and 0.22 and crystallinity  $\geq 3\%$ , 37% and 21%) can be successfully manufactured in this process. These models, techniques, and materials will be applied in a real plant in the future.

#### Acknowledgements

The authors would like to gratefully acknowledge the Center for Micro/Nano Science and Technology, and the National Science Council of the Republic of China (NSC 100-2221-E-006-056-MY3, NSC 102-2622-E-006-012-CC2, NSC 102-2120-M-006-004, and



NSC 102-3113-E-024-001-CC2), Ministry of Economic Affairs of the Republic of China (TDPA: 101-EC-17-A-08-S1-204) for their financial support.

## References

- [1] D.H. Reneker, A.L. Yarin, Electrospinning jets and polymer nanofibers, *Polymer* 49 (10) (2008) 2387–2425.
- [2] M.R. Badrossamay, H.A. McIlwee, J.A. Goss, K.K. Parker, Nanofiber assembly by rotary jet-spinning, *Nano Lett.* 10 (6) (2010) 2257–2261.
- [3] K. Sarkar, C. Gomez, S. Zambrano, M. Ramirez, E. de Hoyos, H. Vasquez, K. Lozano, Electrospinning to forcespinning™, *Mater. Today* 13 (11) (2010) 12–14.
- [4] B.-S. Lee, S.-B. Son, K.-M. Park, W.-R. Yu, K.-H. Oh, S.-H. Lee, Anodic properties of hollow carbon nanofibers for Li-ion battery, *J. Power Sources* 199 (2012) 53–60.
- [5] K. Desai, K. Kit, J. Li, P. Michael Davidson, S. Zivanovic, H. Meyer, Nanofibrous chitosan non-wovens for filtration applications, *Polymer* 50 (15) (2009) 3661–3669.
- [6] S. Wongsasulak, K.M. Kit, D.J. McClements, T. Yoovidhya, J. Weiss, The effect of solution properties on the morphology of ultrafine electrospun egg albumen-PEO composite fibers, *Polymer* 48 (2) (2007) 448–457.
- [7] H. Nie, A. He, B. Jia, F. Wang, Q. Jiang, C.C. Han, A novel carrier of radionuclide based on surface modified poly(lactide-co-glycolide) nanofibrous membrane, *Polymer* 51 (15) (2010) 3344–3348.
- [8] P.-O. Rujitanaroj, N. Pimpha, P. Supaphol, Wound-dressing materials with antibacterial activity from electrospun gelatin fiber mats containing silver nanoparticles, *Polymer* 49 (21) (2008) 4723–4732.
- [9] M.V. Jose, V. Thomas, D.R. Dean, E. Nyairo, Fabrication and characterization of aligned nanofibrous PLGA/Collagen blends as bone tissue scaffolds, *Polymer* 50 (15) (2009) 3778–3785.
- [10] M. Wang, H. Singh, T.A. Hatton, G.C. Rutledge, Field-responsive superparamagnetic composite nanofibers by electrospinning, *Polymer* 45 (16) (2004) 5505–5514.
- [11] K.D. Anderson, D. Lu, M.E. McConney, T. Han, D.H. Reneker, V.V. Tsukruk, Hydrogel microstructures combined with electrospun fibers and photopatterning for shape and modulus control, *Polymer* 49 (24) (2008) 5284–5293.
- [12] A. Greiner, J.H. Wendorff, Electrospinning: a fascinating method for the preparation of ultrathin fibers, *Angew. Chem. Int. Ed.* 46 (30) (2007) 5670–5703.
- [13] P. Katta, M. Alessandro, R.D. Ramsier, G.G. Chase, Continuous electrospinning of aligned polymer nanofibers onto a wire drum collector, *Nano Lett.* 4 (11) (2004) 2215–2218.
- [14] C.Y. Xu, R. Inai, M. Kotaki, S. Ramakrishna, Aligned biodegradable nanofibrous structure: a potential scaffold for blood vessel engineering, *Biomaterials* 25 (5) (2004) 877–886.
- [15] P.D. Dalton, D. Klee, M. Möller, Electrospinning with dual collection rings, *Polymer* 46 (3) (2005) 611–614.
- [16] D. Li, Y. Wang, Y. Xia, Electrospinning of polymeric and ceramic nanofibers as uniaxially aligned arrays, *Nano Lett.* 3 (8) (2003) 1167–1171.
- [17] J.M. Deitzel, J.D. Kleinmeyer, J.K. Hirvonen, N.C. Beck Tan, Controlled deposition of electrospun poly(ethylene oxide) fibers, *Polymer* 42 (19) (2001) 8163–8170.
- [18] M.-S. Khil, S.R. Bhattarai, H.-Y. Kim, S.-Z. Kim, K.-H. Lee, Novel fabricated matrix via electrospinning for tissue engineering, *J. Biomed. Mater. Res. Part B: Appl. Biomater.* 72B (1) (2005) 117–124.
- [19] O.O. Dosunmu, G.G. Chase, W. Kataphinan, D.H. Reneker, Electrospinning of polymer nanofibers from multiple jets on a porous tubular surface, *Nanotechnology* 17 (4) (2006) 1123–1127.
- [20] A.L. Yarin, E. Zussman, Upward needleless electrospinning of multiple nanofibers, *Polymer* 45 (9) (2004) 2977–2980.
- [21] S. Mahalingam, M. Edirisinghe, Forming of polymer nanofibers by a pressurised gyration process, *Macromol. Rapid Commun.* 34 (14) (2013) 1134–1139.
- [22] G. Taylor, Electrically driven jets, *Proc. R. Soc. A: Math. Phys. Eng. Sci.* 313 (1515) (1969) 453–475.
- [23] D.A. Saville, Electrohydrodynamics: the Taylor–Melcher leaky dielectric model, *Annu. Rev. Fluid Mech.* 29 (1997) 27–64.
- [24] A.F. Spivak, Y.A. Dzenis, Asymptotic decay of radius of a weakly conductive viscous jet in an external electric field, *Appl. Phys. Lett.* 73 (21) (1998) 3067–3069.
- [25] M.M. Hohman, M. Shin, G. Rutledge, M.P. Brenner, Electrospinning and electrically forced jets: I. Stability theory, *Phys. Fluids* 13 (8) (2001) 2201–2220.
- [26] M.M. Hohman, M. Shin, G. Rutledge, M.P. Brenner, Electrospinning and electrically forced jets: II. Applications, *Physics of Fluids* 13 (8) (2001) 2221–2236.
- [27] D.H. Reneker, A.L. Yarin, H. Fong, S. Koombhongse, Bending instability of electrically charged liquid jets of polymer solutions in electrospinning, *J. Appl. Phys.* 87 (9) (2000) 4531–4547.
- [28] A.L. Yarin, S. Koombhongse, D.H. Reneker, Bending instability in electrospinning of nanofibers, *J. Appl. Phys.* 89 (5) (2001) 3018–3026.
- [29] J.J. Feng, Stretching of a straight electrically charged viscoelastic jet, *J. Non-Newtonian Fluid Mech.* 116 (1) (2003) 55–70.
- [30] S.V. Fridrikh, J.H. Yu, M.P. Brenner, G.C. Rutledge, Controlling the fiber diameter during electrospinning, *Phys. Rev. Lett.* 90 (14) (2003) 144502–1–144502–4.
- [31] A.F. Spivak, Y.A. Dzenis, D.H. Reneker, A model of steady state jet in the electrospinning process, *Mech. Res. Commun.* 27 (1) (2000) 37–42.
- [32] J.A. Matthews, G.E. Wnek, D.G. Simpson, G.L. Bowlin, Electrospinning of collagen nanofibers, *Biomacromolecules* 3 (2) (2002) 232–238.
- [33] M.V. Kakade, S. Givens, K. Gardner, K.H. Lee, D. Bruce Chase, J.F. Rabolt, Electric field induced orientation of polymer chains in macroscopically aligned electrospun polymer nanofibers, *J. Am. Chem. Soc.* 129 (10) (2007) 2777–2782.
- [34] T. Kongkhlang, K. Tashiro, M. Kotaki, S. Chirachanchai, Electrospinning as a new technique to control the crystal morphology and molecular orientation of polyoxymethylene nanofibers, *J. Am. Chem. Soc.* 130 (46) (2008) 15460–15466.
- [35] J.J. Feng, The stretching of an electrified non-Newtonian jet: a model for electrospinning, *Phys. Fluids* 14 (11) (2002) 3912–3926.
- [36] M.E. Helgeson, N.J. Wagner, A correlation for the diameter of electrospun polymer nanofibers, *AIChE J.* 52 (1) (2007) 51–55.
- [37] C.-C. Liao, S.-S. Hou, C.-C. Wang, C.-Y. Chen, Electrospinning fabrication of partially crystalline bisphenol A polycarbonate nanofibers: the effects of molecular motion and conformation in solutions, *Polymer* 51 (13) (2010) 2887–2896.
- [38] C.-C. Liao, C.-C. Wang, K.-C. Shih, C.-Y. Chen, Electrospinning fabrication of partially crystalline bisphenol A polycarbonate nanofibers: effects on conformation, crystallinity, and mechanical properties, *Eur. Polym. J.* 47 (5) (2011) 911–924.
- [39] C.-C. Liao, C.-C. Wang, C.-Y. Chen, Stretching-induced crystallinity and orientation of polylactic acid nanofibers with improved mechanical properties using an electrically charged rotating viscoelastic jet, *Polymer* 52 (19) (2011) 4303–4318.
- [40] C.-C. Liao, C.-C. Wang, C.-Y. Chen, W.-J. Lai, Stretching-induced orientation of polyacrylonitrile nanofibers by an electrically rotating viscoelastic jet for improving the mechanical properties, *Polymer* 52 (10) (2011) 2263–2275.
- [41] Y.-H. Liang, C.-C. Wang, C.-Y. Chen, The conductivity and characterization of the plasticized polymer electrolyte based on the P(AN-co-GMA-IDA) copolymer with chelating group, *J. Power Sources* 148 (15) (2005) 55–65.
- [42] S.-H. Lee, C. Tekmen, W.M. Sigmund, Three-point bending of electrospun TiO<sub>2</sub> nanofibers, *Mater. Sci. Eng.: A* 398 (1–2) (2005) 77–81.
- [43] E.P.S. Tan, C.T. Lim, Physical properties of a single polymeric nanofiber, *Appl. Phys. Lett.* 84 (9) (2004) 1603–1605.
- [44] M.K. Shin, S.I. Kim, S.J. Kim, Reinforcement of polymeric nanofibers by ferritin nanoparticles, *Appl. Phys. Lett.* 88 (19) (2006) 193901–1–193901–3.
- [45] J.G. Lawrence, L.M. Berhan, A. Nadarajah, Elastic properties and morphology of individual carbon nanofibers, *ACS Nano* 2 (6) (2008) 1230–1236.
- [46] Q. Cheng, S. Wang, D.P. Harper, Effects of process and source on elastic modulus of single cellulose fibrils evaluated by atomic force microscopy, *Compos. Part A: Appl. Sci. Manuf.* 40 (5) (2009) 583–588.
- [47] B.J. Briscoe, L. Fiori, E. Pelillo, Nano-indentation of polymeric surfaces, *J. Phys. D: Appl. Phys.* 31 (19) (1999) 2395–2405.
- [48] X. Li, H.-S. Gao, C.J. Murphy, K.K. Caswell, Nanoindentation of silver nanowires, *Nano Lett.* 3 (11) (2003) 1495–1498.
- [49] X. Li, H.-S. Gao, C.J. Murphy, L. Gou, Nanoindentation of Cu<sub>2</sub>O nanocubes, *Nano Lett.* 4 (10) (2004) 1903–1907.
- [50] W.C. Oliver, G.M. Pharr, An improved technique for determining hardness and elastic modulus using load and displacement sensing indentation experiments, *J. Mater. Res.* 7 (6) (1992) 1564–1583.
- [51] G.M. Pharr, A. Bolshakov, Understanding nanoindentation unloading curves, *J. Mater. Res.* 17 (10) (2002) 2660–2671.
- [52] G.K. Batchelor, An Introduction to Fluid Dynamics, Cambridge Mathematical Library, 1967.
- [53] H. David, R. Robert, W. Jearl, Fundamentals of Physics, John Wiley & Sons Inc., 2007.
- [54] E.I. Părău, S.P. Decent, M.J.H. Simmons, D.C.Y. Wong, A.C. King, Nonlinear viscous liquid jets from a rotating orifice, *J. Eng. Math.* 57 (2) (2007) 159–179.
- [55] G.C. Rutledge, S.V. Fridrikh, Formation of fibers by electrospinning, *Adv. Drug Delivery Rev.* 59 (14) (2007) 1384–1391.